ORIGINAL ARTICLE

Capacitor-less modular multilevel converter with sliding mode control for MV adjustable-speed motor drives

Mohamed Atef Tawfik[1] · Mohammad Sameer Irfan[1] · Chungu Lee[1] · Ashraf Ahmed[1] · Joung-Hu Park[1]

Abstract

Medium-voltage (MV) motor drives have become an appealing application for modular multilevel converters (MMCs). Starting and operation at low speeds result in wide fluctuations of the low-frequency ripple components in the sub-module (SM) capacitors DC link voltages, which can adversely affect system performance and system lifetime. A solution for this problem is to replace the low-frequency (LF) SM capacitor with a power decoupling circuit (PDC) that is independent from the converter line frequency. In this paper, a power decoupling approach based on the flux cancelation method is proposed. A three-winding high-frequency transformer (HFT) is employed to magnetically couple and cancel the three-phase symmetrical ripple power. However, this approach has two main challenges. (1) The ripple powers through the HFT are a function of the value of the leakage inductances. (2) Different leakage inductances and ripple power unbalance between phases cause unequal ripple voltages. As a result, phase-shift ripple rejection control is needed. Conventional liner controllers have several problems, such as bandwidth limitations, stability margins, and slow dynamics near-zero-speed operation. In addition, linear controllers are designed for a specific ripple frequency. In this paper, a frequency-independent ripple rejection sliding mode controller (SMC) is proposed to overcome the limitations of linear controllers. The SMC is applied to pass the SM capacitor voltage ripple into the HFT. Thus, the ripple is canceled out in the HFT magnetic core regardless of the converter line frequency. The proposed control is suitable for adjustable-speed applications. The performance of the proposed scheme is verified via simulation and experimental tests.

Keywords MMC · Power decoupling · Capacitor voltage ripple · MV variable-speed drives · Sliding mode control

1 Introduction

The modular multilevel converter (MMC) is considered to be one of the most promising topologies for medium-voltage high-power industrial applications, such as the powertrains of electric vehicle motor drives, due to its modularity, scalable voltage level, single DC bus, etc. [1–3].

However, the MMC has an inherent issue with the SM capacitor voltage low-frequency ripple components dramatically increasing when the operating line frequency is reduced, which can adversely affect the system performance and lifetime. This issue limits the application of MMCs in variable-speed machine drives [4].

✉ Joung-Hu Park
   wait4u@ssu.ac.kr

1 Department of Electrical Engineering, Soongsil University, Seoul, Republic of Korea

Several approaches have been proposed in the literature to address this serious issue [5–11]. In [5, 6, 9, 10], different power-balancing channels were proposed to balance the voltage ripple between the MMC arms by transferring the ripple power from the arm that has the largest ripple to the other arms, which can increase the circuit components ratings. In addition, several of these techniques only compensate the fundamental frequency ripple power component when the double-fundamental frequency component is kept uncompensated. In [7, 8], an additional active power filter was connected to each of the SMs of a MMC to direct the ripple power to a low-frequency capacitor. However, the increase in the part count was significant. In addition, these approaches use large LF capacitors.

In this paper, a frequency-independent magnetic power decoupling circuit (PDC) is proposed to replace the LF SM capacitor. The proposed approach compensates for both the fundamental and the double-fundamental ripple power components in the MMC arms. Figure 1 shows a MMC
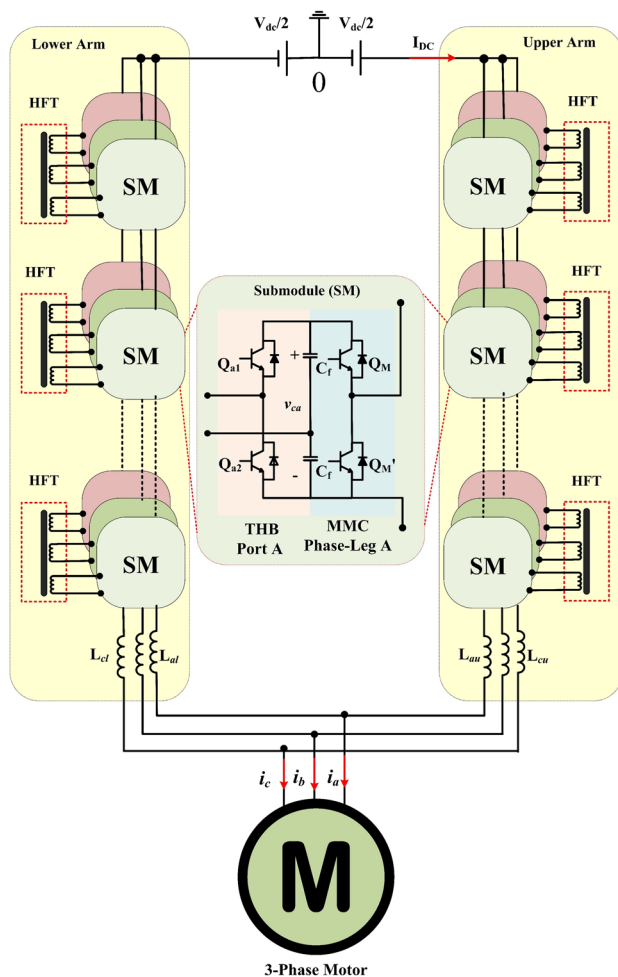
Fig. 1 MMC with a THB-based power decoupling circuit

with a power decoupling configuration. The MMC-SM is a two-half-bridge (HB) with a very small high-frequency film capacitor as a DC link. Each of the symmetrically modulated adjacent-arm SMs is magnetically coupled to decouple the three-phase ripple power. The PDC is realized through a three-winding HFT with three-port half-bridge (THB) converters interfacing each of the three-phase contiguous SMs. The three-phase PDC is theoretically based on the flux cancelation method. Its basic idea is to eliminate the three-phase symmetrical modulation ripple powers since their instantaneous sum is zero. Instantaneous three-phase ripple power gathering occurs magnetically in the HFT core.

The amount of ripple power sent to the HFT through the power de-coupler depends on the leakage inductance of the transformer and the phase shift. A phase-shift controller is needed to drive the pulsating power toward the HFT to ensure an acceptable capacitor voltage ripple level. Different ripple rejection control methods were proposed in [12–16]. One of these methods involved a dual control loop [12], where the outer loop provides voltage with a crossover

frequency far below that of the ripple component frequency, and the inner loop provides current feedback with a wider bandwidth. The narrow bandwidth of the voltage loop degrades the dynamic response of the system and introduces instability. In [13], a notch filter was inserted into the voltage loop to enhance the voltage loop bandwidth. However, this added a large negative phase shift in some frequencies lower than the filter cut-off frequency, which can reduce the phase margin of the system [14]. Other papers have proposed a converter impedance-shaping method to block the ripple components [15, 16]. These approaches were designed for a specific frequency, which makes them unsuitable for variable frequency applications and variable-speed applications. Furthermore, some of the aforementioned approaches degrade the dynamic performance of the system. All of these approaches use a linear controller, which has limitations in terms of robustness and stability.

This paper proposes a sliding mode controller (SMC) that regulates the wide variations in the system parameters, and it is more suitable for variable structure systems such as power electronic converters [17–25]. The SMC for a PDC is designed to shape the input impedance of the THB converter, and it enforces the delivery of ripple power to the high-frequency transformer to be canceled on the HFT core. The SMC is independent of the MMC ripple frequency, unlike conventional methods such as proportional resonance (PR) controllers, which are designed for the ripple frequency. The proposed SMC can keep the capacitor voltage ripple of the SM narrow from standstill to full speed, without the need for a filtering stage. This means it does not suffer from stability limitations as with conventional control methods. The proposed SMC method ensures system robustness against variations in the circuit parameters. Furthermore, it has a faster transient response with negligible overshoots and undershoots. The control design is also introduced in this paper. Additionally, the system stability under SMC is analyzed. The robustness of the proposed control against system parameter variations is demonstrated.

1.1 Motivations

The SM capacitor voltage of a MMC suffers from LF ripple components, where their magnitude is inversely proportional to the line frequency of the converter. Therefore, utilizing a MMC in adjustable-speed applications is a challenge. Employing a magnetic PDC instead of a bulky SM capacitor is a solution for this issue. A fast and robust ripple rejection control is needed for the PDC. The main issue with variable-speed motor drive applications is that there is a need for variable frequency control. Therefore, conventional PR-based controllers are problematic since a large number of PR controllers are needed, or a large number of complex adaptive filters are needed if d–q control was used. The conventional

linear ripple rejection methods suffer from bandwidth and stability limitations. Additionally, at near-zero-speed operation, the PR controller has slower dynamics. Therefore, a fast nonlinear ripple rejection control is proposed for the PDC. The proposed control is independent of the ripple frequency. Therefore, the proposed scheme can drive medium-voltage high-power variable-speed machines from standstill to full speed with a narrow SM capacitor voltage ripple.

1.2 Challenges

1. Modeling a three-port power decoupling circuit is a challenge since the circuit has three input ports and zero output ports.
2. Keeping the conventional MMC sensing points the same without adding extra sensing points is difficult.
3. Designing a nonlinear ripple rejection control that can overcome linear control limitations is challenging.

1.3 Contributions

1. The proposed scheme solves the issue of wide fluctuations of the low-frequency voltage ripple components in SM capacitors, especially under low-speed operations without using a bulky ripple power capacitor.
2. The proposed scheme succeeds in keeping the SM capacitor voltage ripple narrow regardless of the converter line frequency.
3. The modeling of the THB-based power decoupling circuit has the following enhancements.

   (a) A novel transient model was applied to the THB-based power decoupling circuit, which is based on the state space generalized average modeling.
   (b) This model provides a highly accurate modeling of the system dynamics.

4. The proposed sliding mode control offers the following enhancements.

   (a) Conventional ripple rejection controllers are designed with a crossover frequency that is far below that of the ripple component which can degrade the system dynamics and introduce instability, especially under low-frequency operation. However, the proposed control has nonlinear design that is independent of the ripple frequency, which solves these issues.
   (b) There is no need for adaptive filters or a large number of PR controllers, which makes it less complicated in comparison with conventional methods.

   (c) It compensates both the differential mode and the common mode ripple components of the SM capacitors.
   (d) No extra sensors are required since it is current sensor-less control.
   (e) Robust control against system parameter variations.
   (f) It is a frequency-independent control. Therefore, it suitable for both adjustable-speed and low-speed operations.

The remainder of this paper is organized as follows. Section 2 introduces the proposed model of a power decoupling circuit-based THB converter. Section 3 describes the proposed sliding mode controller. In Sect. 4, the proposed scheme performance is verified by simulation and experimental tests. Section 5 discusses the system volume reduction when compared to conventional methods. Section 6 provides some concluding remarks.

2 Proposed circuit modeling

Figure 2 shows a detailed circuit diagram of a THB-based power decoupling circuit in symmetrically modulated three-phase MMC legs. The THB extracts the instantaneous ripple power from the SMs, and pushes it to the HFT. The ripple power flows from each of the THB ports to the three-winding HFT are canceled out in the magnetic core.

The modeling procedures of the power decoupling circuit are proposed, and the derived model is used to estimate the transformer currents. Due to three-phase symmetry, the circuit in Fig. 2 is modeled, and the model is extended to any group of three contiguous arm SMs. In the proposed THB, the ripple power flows from all three of the ports to the single three-winding HFT. To date, no literature reports have addressed the modeling of this type of circuit. Figure 3 shows an equivalent circuit of the three-port PDC shown in Fig. 2. The inverter side of the MMC is modeled with three parallel current sources i_{sJ} with a resistance R_J. The HFT is modeled with a T-model. The HFT windings are modeled
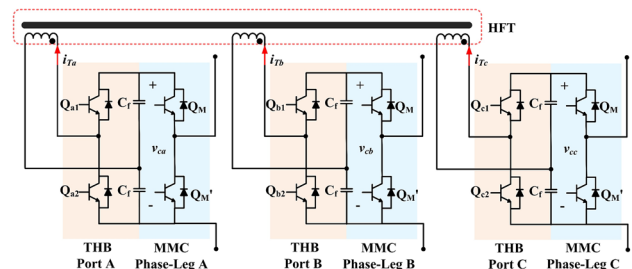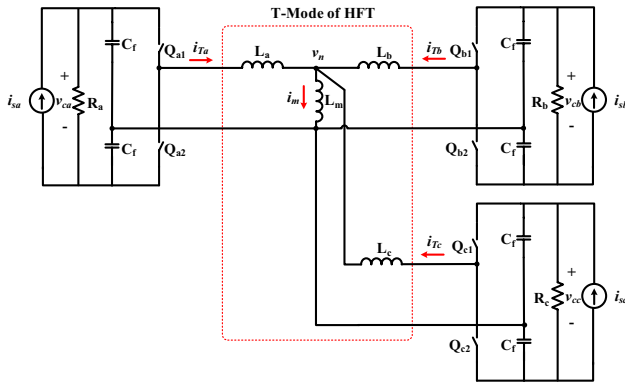

Fig. 2 Three contiguous MMC arm SMs

Fig. 3 Equivalent circuit of the three-phase contiguous SMs of a MMC

with their leakage inductance L_J, and the core is modeled with the magnetizing inductance L_m, which has a current i_m and a voltage drop v_n. The equivalent circuit shown in Fig. 3 has two operational modes. The combined form of the switched model can be defined as follows:

$$\frac{di_{TJ}}{dt} = \frac{1}{2L_J}u_J v_{cJ} - \frac{1}{L_J}v_n, \tag{1}$$

$$\frac{dv_{cJ}}{dt} = \frac{2}{c_f}i_{sJ} - 2\frac{v_{cJ}}{R_J c_f} - \frac{1}{c_f}u_J i_{TJ}, \tag{2}$$

$$\frac{di_m}{dt} = \frac{1}{L_m}v_n. \tag{3}$$

where $u = [1, 0]$ and $J = \{a, b, c\}$.

GAM is used to average the previously derived switched model, as can be seen in (1)–(3). The GAM is based on waveform representation employing the complex Fourier series [26]. After a mathematical derivation, the complex state space representation per phase of the circuit in Fig. 3 is obtained as follows:

$$\frac{di_{TJR}}{dt} = \frac{1}{\pi L_J}v_{cJ}\sin(\varnothing_J) - \frac{1}{L_J}v_{nR} + \omega_s i_{TJI} \tag{4}$$

$$\frac{di_{mR}}{dt} = \frac{1}{L_m}v_{nR} + \omega_s i_{mI} \tag{5}$$

$$\frac{dv_{cJ}}{dt} = \frac{2}{c_f}i_{sJ} - 2\frac{v_{cJ}}{R_J c_f} - \frac{4}{\pi c_f}\sin(\varnothing_J)i_{TJR} + \frac{4}{\pi c_f}\cos(\varnothing_J)i_{TJI} \tag{6}$$

$$\frac{di_{TJI}}{dt} = -\frac{1}{\pi L_J}v_{cJ}\cos(\varnothing_J) - \frac{1}{L_J}v_{nI} - \omega_s i_{TJR} \tag{7}$$

$$\frac{di_{mI}}{dt} = \frac{1}{L_m}v_{nI} - \omega_s i_{mR} \tag{8}$$

where $\omega_s = 2\pi f_s$, and f_s is the switching frequency. $\varnothing_J$ is the phase shift angle. i_{TJR}, i_{mR}, and v_{nR} are the real parts of the first harmonic component of the transformer current, the transformer magnetizing current, and the transformer magnetizing voltage, respectively. i_{TJI}, i_{mI}, and v_{nI} are the imaginary parts of the first harmonic component of the transformer current, transformer magnetizing current, and transformer magnetizing voltage, respectively.

Normally, current is used as a control variable to design a fast response controller. However, the transformer currents are high-frequency currents. Sensing high-frequency currents requires high bandwidth sensors and a fast DSP, which increases the cost of the system. A solution is to estimate the currents rather than sense them. For this estimation, (4)–(8) can be rewritten as:

$$\frac{di_{TJR}}{dt} = X_{J1}\sin(\varnothing_a)v_{ca} + X_{J2}\sin(\varnothing_b)v_{cb} + X_{J3}\sin(\varnothing_c)v_{cc} + X_{J4}i_{TjI} \tag{9}$$

$$\frac{di_{TJI}}{dt} = -X_{J1}\cos(\varnothing_a)v_{ca} - X_{J2}\cos(\varnothing_b)v_{cb} - X_{J3}\cos(\varnothing_c)v_{cc} - X_{J4}i_{TjR} \tag{10}$$

where $X_{a1} = X_{b2} = X_{c3} = \frac{1}{\pi L}(\frac{L+2L_m}{L+3L_m})$, $X_{a1} = X_{b2} = X_{c3} = \omega_s$, and $X_{a2,3} = X_{b1,3} = X_{c1,3} = -\frac{1}{\pi L}(\frac{1}{L+3L_m})$. For the sake of simplicity, $L_a = L_b = L_c = L$ was chosen. A block diagram of the current estimator per phase is shown in Fig. 4.

3 Proposed sliding mode control

Figure 5 shows the proposed control scheme for a MMC drive three-phase machine. The overall control scheme can be divided into the following three main parts. (1) Motor control is applied to control the motor operation characteristics (torque and speed). (2) MMC control is applied to control the MMC performance. (3) PDC control is applied to keep the SM capacitor voltage ripple narrow. In this section, sliding mode control is introduced for the PDC. The other control parts are described in [3–10, 27]. The sliding mode controller is proposed for the THB circuit to force the ripple power to flow to the HFT to be canceled out in the core. Sliding mode control is a variable structure control that is resistant to system disturbances and parameter uncertainties. Its implementation is less complex when compared to other nonlinear controls. In the following, the sliding mode control design steps are given.
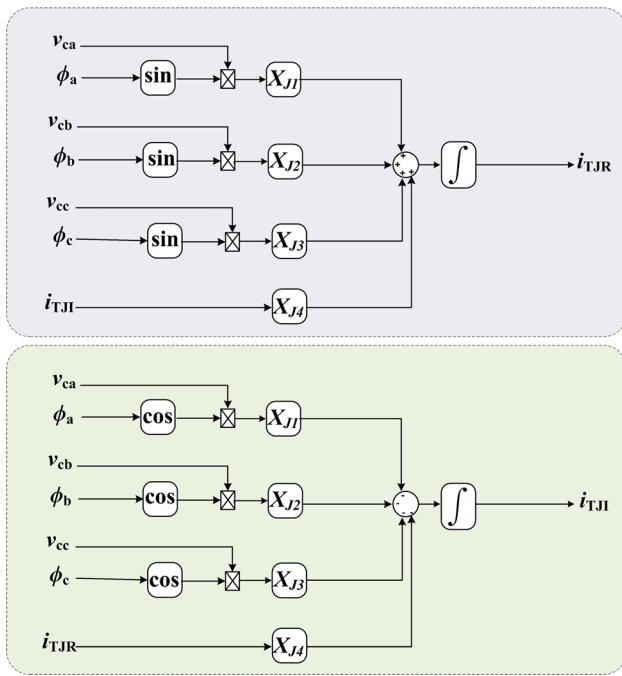
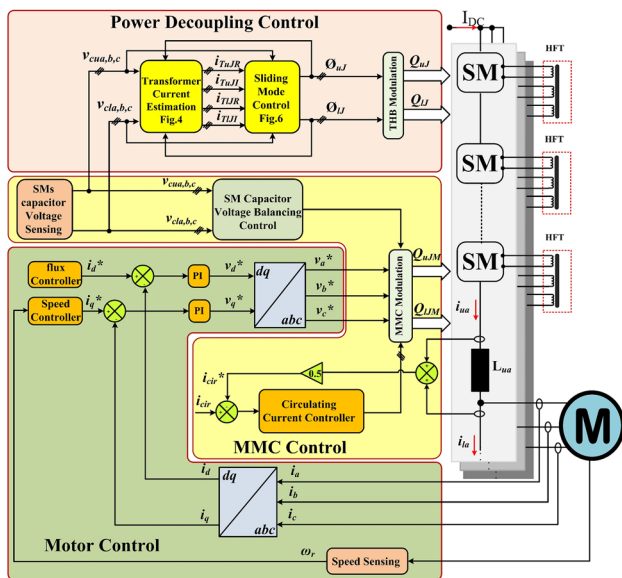**Fig. 4** Block diagram of a transformer currents estimator

Fig. 5 Proposed control scheme (the subscripts "*u*" and "*l*" stand for upper and lower arms, respectively)

3.1 Proposed control design

To design the proposed sliding mode controller, the sliding surface should be selected according to the control objectives. In this paper, the sliding surface s_J is chosen as a function of the transformer current as follows:

$$s_J = -k_1 \frac{\mathrm{d}i_{TJR}}{\mathrm{d}t} - \frac{1}{k_2} \int i_{TJR}\mathrm{d}t - k_3 i_{TJR} \tag{11}$$

where k_1, k_2, and k_3 are design parameters. Once the state trajectory reaches the sliding surface, it should slide along the surface toward the equilibrium point. The sliding mode phase operation can be described by constant dynamics [19]:

$$\frac{\mathrm{d}s_J}{\mathrm{d}t} = 0 \tag{12}$$

where the time derivative of s_J is:

$$\frac{\mathrm{d}s_J}{\mathrm{d}t} = -k_1 \frac{\mathrm{d}^2 i_{TJR}}{\mathrm{d}t^2} - \frac{1}{k_2} i_{TJR} - k_3 \frac{\mathrm{d}i_{TJR}}{\mathrm{d}t} \tag{13}$$

Replacing $\frac{\mathrm{d}i_{TJR}}{\mathrm{d}t}$ in (13) with (4) yields the following equation:

$$\frac{\mathrm{d}s_J}{\mathrm{d}t} = -k_1 \frac{\mathrm{d}^2 i_{TJR}}{\mathrm{d}t^2} - \frac{1}{k_2} i_{TJR} - k_3 \left(\frac{1}{\pi L_J} v_{cJ} \sin(\varnothing_J) - \frac{v_{nR}}{L_J} + \omega_s i_{TJI} \right) \tag{14}$$

In addition, using (12) and (14), the equivalent control part is obtained as follows:

$$\varnothing_{J\,\mathrm{eq}} = \sin^{-1}\left(\frac{\pi L_J}{v_{cJ}} \left(-\frac{k_1}{k_3} \frac{\mathrm{d}^2 i_{TJR}}{\mathrm{d}t^2} - \frac{1}{k_3 k_2} i_{TJR} + \frac{v_{nR}}{L_J} - \omega_s i_{TJI} \right) \right) \tag{15}$$

The reaching dynamics have been chosen as follows:

$$\frac{\mathrm{d}s_J}{\mathrm{d}t} = -\Gamma s_J - \alpha \cdot \mathrm{sign}(s_J) \tag{16}$$

which ensures that the state trajectory reaches $s = 0$ in a finite time. The phase-shift expiration is then:

$$\varnothing_J = \sin^{-1}\left(\frac{\pi L_J}{v_{cJ}} \left(-\frac{k_1}{k_3} \frac{\mathrm{d}^2 i_{TJR}}{\mathrm{d}t^2} - \frac{1}{k_3 k_2} i_{TJR} + \frac{1}{L_J} v_{nR} - \omega_s i_{TJI} + \Gamma s_J + \alpha\,\mathrm{sign}(s_J) \right) \right) \tag{17}$$

The following condition must always be investigated:

$$-1 \le \frac{\pi L_J}{v_{cJ}} \left(-\frac{k_1}{k_3} \frac{\mathrm{d}^2 i_{TJR}}{\mathrm{d}t^2} - \frac{1}{k_3 k_2} i_{TJR} + \frac{1}{L_J} v_{nR} - \omega_s i_{TJI} + \Gamma s_J + \alpha\,\mathrm{sign}(s_J) \right) \tag{18}$$

Figure 6 shows a block diagram of the proposed sliding mode control, as can be seen in (17).

To ensure that the sliding surface is an attractor to the state trajectory, the following existence conditions should be valid in the neighborhood of the sliding manifold. This allows it to fulfill the local reachability condition [21].

$$s_J \frac{\mathrm{d}s_J}{\mathrm{d}t} < -\eta |s_J|, \eta > 0 \tag{19}$$

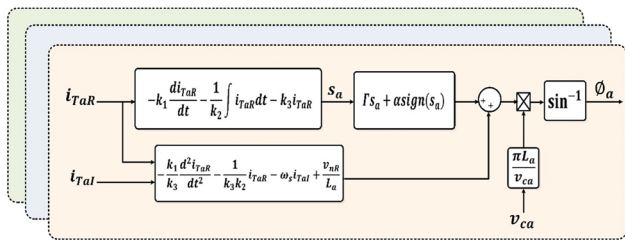Recalling the reaching dynamics (16), the local reachability condition is:

Fig. 6 Block diagram of the proposed sliding mode control for a THB circuit

$$s_J \frac{\mathrm{d}s_J}{\mathrm{d}t} = -\left(\Gamma|s_J| + \alpha\right)|s_J| \tag{20}$$

Comparing (19) with (20), yields $\eta \geq \Gamma|s_J| + \alpha$. Thus, the existence condition for the sliding mode is $\eta > \Gamma|s_J| + \alpha$ at $\Gamma, \alpha > 0$.

3.2 Sliding mode stability analysis

The following ideal sliding-mode dynamics represent the reduced-order dynamics of the system on the sliding surface.

$$\frac{\mathrm{d}v_{cJ}}{\mathrm{d}t} = -2\frac{v_{cJ}}{R_J c_f} - \frac{4}{\pi}c_f \sin\left(\varnothing_{J\mathrm{eq}}\right)i_{TJR} + \frac{4}{\pi c_f}\cos\left(\varnothing_{J\mathrm{eq}}\right)i_{TJI} \tag{21}$$

$$\frac{\mathrm{d}i_{TJI}}{\mathrm{d}t} = -\frac{1}{\pi L_J}v_{cJ}\cos\left(\varnothing_{J\mathrm{eq}}\right) - \omega_s i_{TJR} - \frac{1}{L_J}v_{n\mathrm{I}} \tag{22}$$

The equilibrium point can be obtained by forcing the left side of (21) and (22) to be equal to zero. Then the two equations are solved to obtain the steady state value of the two components of the transformer current (I_{TJI} and I_{TJR}), where the steady values of v_{cJ}, $v_{n\mathrm{I}}$, $v_{n\mathrm{R}}$, and $\varnothing_{J\mathrm{eq}}$ are V_{cJ}, $V_{n\mathrm{I}}$, $V_{n\mathrm{R}}$, and $\Psi_{J\mathrm{eq}}$, respectively. The Routh-Hurwitz stability criterion is applied to (21) and (22) to verify the system stability on the sliding phase. The linearized (21) and (22) around the equilibrium point is:

$$\begin{bmatrix} \frac{\mathrm{d}v_{cJ}}{\mathrm{d}t} \\ \frac{\mathrm{d}i_{TJI}}{\mathrm{d}t} \end{bmatrix} = A \begin{bmatrix} \hat{v}_{cJ} \\ \hat{i}_{TJI} \end{bmatrix} \tag{23}$$
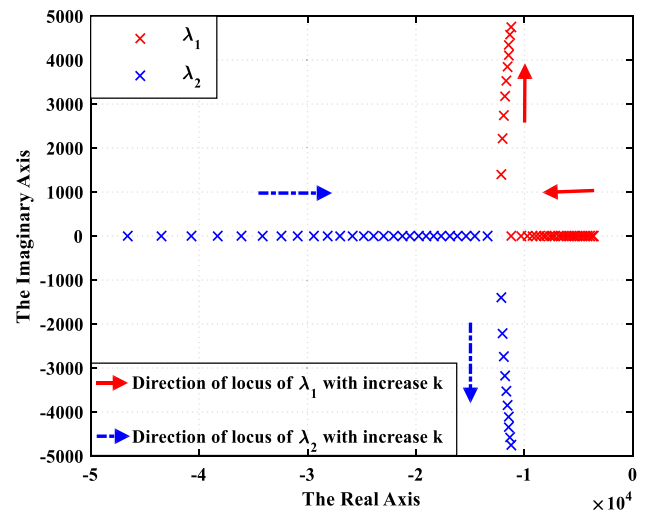

Fig. 7 Locus of eigenvalues with changing sliding surface gains

where A is the Jacobean matrix of the system around the equilibrium point and for some (k_1, k_2, k_3). A is the following matrix (see the bottom of this page (24)). The A matrix in (24) can be rewritten in a more general form as follows:

$$A = \begin{bmatrix} a_{11} & a_{12} \\ a_{21} & a_{22} \end{bmatrix}$$

$$A = \begin{bmatrix} -\frac{2}{R_J c_f} + \frac{4\tan(\Psi_{J\mathrm{eq}})}{\pi c_f V_{cJ}}\left(I_{TJR}\cos\left(\Psi_{J\mathrm{eq}}\right) + I_{TJI}\sin\left(\Psi_{J\mathrm{eq}}\right)\right) & \frac{4}{\pi c_f}\cos\left(\Psi_{J\mathrm{eq}}\right) + \frac{4L_J\omega_s}{c_f V_{cJ}}\left(I_{TJR} + I_{TJI}\tan(\Psi_{J\mathrm{eq}})\right) \\ -\frac{1}{\pi L_J}\cos\left(\Psi_{J\mathrm{eq}}\right) - \frac{1}{\pi L_J}\sin\left(\Psi_{J\mathrm{eq}}\right)\tan(\Psi_{J\mathrm{eq}}) & -\omega_s\tan(\Psi_{J\mathrm{eq}}) \end{bmatrix} \tag{24}$$

The characteristic equation of the system ($|\lambda I - A| = 0$) is:

$$\lambda^2 - \left(a_{11}s + a_{22}\right)\lambda + a_{11}a_{22} - a_{12}a_{21} = 0 \tag{25}$$

Finally, by applying the Routh–Hurwitz stability criterion to this second-order linear polynomial, it is found that all of the coefficients must be positive, i.e., $k_1, k_2, k_3 > 0$, to ensure that all of the eigenvalues of the system have a negative real part [20].

Figure 7 shows the locus of the eigenvalues (λ_1, λ_2) with increasing sliding surface gains, where $k = k_2 k_3$. In addition, k_1 has a negligible effect. It can be observed that the system is stable since all of the eigenvalues are in the left side plane. Therefore, for low values of (k), the eigenvalues are real and negative. Thus, the system is critically damped [20]. This indicates that the system performs better at low values of (k).

3.3 THB Impedance shaping

To highlight the effectiveness of the proposed sliding mode control, it is shown how the sliding mode control shapes the input side impedance (Z_{in}) of the THB converter to bypass the ripple power to the HFT. Referring to (23) and (24), Z_{in} in the frequency domain can be defined as follows:

$$Z_{in} = \frac{\frac{4}{\pi c_f}\cos\left(\Psi_{Jeq}\right) + \frac{4L_J\omega_s}{c_f V_{cJ}}\left(I_{TJR} + I_{TJI}\tan(\Psi_{Jeq})\right)}{\lambda + \frac{2}{R_J c_f} - \frac{4\tan(\Psi_{Jeq})}{\pi c_f V_{cJ}}\left(I_{TJR}cos\left(\Psi_{Jeq}\right) + I_{TJI}\sin\left(\Psi_{Jeq}\right)\right)} \quad (26)$$

where λ is a complex number, and $Z_{in} = \frac{\hat{v}_{cJ}}{\hat{i}_{TJI}}$. To obtain the common mode impedance (Z_{CM}) and the differential mode

$$\frac{ds_J}{dt} = -k_1\frac{d^2 i_{TJR}}{dt^2} - \frac{1}{k_2}i_{TJR} - k_3\left(\frac{1}{\pi(L_J + \Delta L_J)}v_{cJ}\sin(\varnothing_J) - \frac{v_{nR}}{(L_J + \Delta L_J)} + \omega_s i_{TJI}\right) \quad (27)$$

$$\frac{ds_J}{dt} = \left(\frac{L_J}{(L_J + \Delta L_J)} - 1\right)\left(-\dot{s}_J - k_3\frac{di_{TJR}}{dt} + k_3\omega_s i_{TJI}\right) - \frac{L_J}{(L_J + \Delta L_J)}\Gamma s_J - \frac{L_J}{(L_J + \Delta L_J)}\alpha sign(s_J) \quad (28)$$

impedance (Z_{DM}), λ is replaced in (26) with the fundamental line frequency and double the line frequency, respectively. Figure 8 shows Z_{DM} and Z_{CM} versus the sliding surface gains (k). From Fig. 8 it can be concluded that the sliding mode control can shape Z_{in}. By varying the sliding surface gains, the amount of ripple power transferred through the THB can
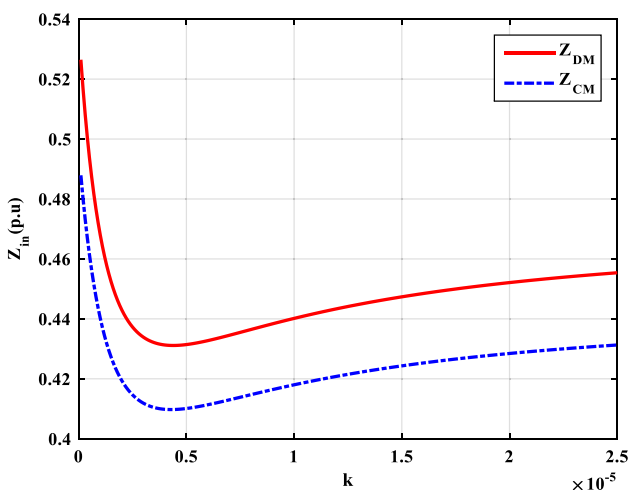
Fig. 8 Shaping the input side impedance (Z_{in}) of a THB converter by changing the sliding surface gains at ($V_{cJ} = 260V, c_f = 30\mu F$, and $L = 100\mu H$)

be controlled. This graphical approach can be used to design the sliding surface gains to achieve optimal values of Z_{DM} and Z_{CM}.

3.4 Robustness analysis

A robustness analysis is performed in the presence of uncertainty in the HFT leakage inductance (L_J). The aim of this analysis is to determine whether the sliding phase $s_J = 0$ is established despite system parameter uncertainty. The sliding phase starts after the local reachability condition is satisfied, and the local reachability condition is defined in Eq. (19). For this, it is necessary to recall Eq. (14) and replace (L_J) with $(L_J + \Delta L_J)$, where (ΔL_J) is the uncertainty in (L_J). Then Eq. (14) can be rewritten as follows:

Using Eqs. (13) and (17), Eq. (27) is:

which leads to:

$$\frac{L_J}{(L_J + \Delta L_J)}\frac{ds_J}{dt} = \left(\frac{\Delta L_J}{(L_J + \Delta L_J)}\right)k_3\frac{di_{TJR}}{dt} + \left(\frac{-\Delta L_J}{(L_J + \Delta L_J)}\right)$$

$$k_3\omega_s i_{TJI} - \frac{L_J}{(L_J + \Delta L_J)}\Gamma s_J - \frac{L_J}{(L_J + \Delta L_J)}\alpha sign(s_J) \quad (29)$$

Dividing both sides of Eq. (29) by $\frac{L_J}{(L_J + \Delta L_J)}$ yields $\frac{ds_J}{dt}$ as follows:

$$\frac{ds_J}{dt} = \Delta x - \Gamma s_J - \alpha sign(s_J) \quad (30)$$

where $\Delta x = \frac{\Delta L_J}{L_J}k_3\frac{di_{TJR}}{dt} - \frac{\Delta L_J}{L_J}k_3\omega_s i_{TJI}$.

The robustness of the control against system parameter variations is ensured if the local reachability condition, as shown in (19), is satisfied. Using Eq. (30), the left term of Eq. (19) is as follows:

$$s_J\frac{ds_J}{dt} = s_J\left(\Delta x - \Gamma s_J - \alpha sign(s_J)\right) \quad (31)$$

Since $s_J sign(s_J) = |s_J|$, Eq. (30) is:

$$s_J\frac{ds_J}{dt} = -\left(-\frac{\Delta x}{sign(s_J)} + \Gamma|s_J| + \alpha\right)|s_J| \quad (32a)$$

$$s_J \frac{\mathrm{d}s_J}{\mathrm{d}t} = -\eta'|s_J| \qquad (32\mathrm{b})$$

where $\eta' = \left(-\frac{\Delta x}{\mathrm{sign}(s_J)} + \Gamma|s_J| + \alpha\right)$.

The reachability condition is satisfied at $\eta' > 0$. It is assumed that $\Delta x = \rho_{\max}$ is the maximum tolerable uncertainty in the system parameters. When using (32) and $\eta' > 0$, the following condition must be fulfilled:

$$|\rho_{\max}| < |\Gamma|s_J| + \alpha| \qquad (33)$$

When $\alpha > \rho_{\max}$ is chosen, the condition given by (33) is satisfied.

4 Verifications

The performance of the proposed scheme is verified using a megawatt simulation system and a downscaled laboratory hardware prototype. The performance is investigated under different operation conditions.

4.1 Simulation verification

The PSIM circuit parameters are shown in Table 1. The circuit has two SMs per phase. Figure 9 shows circuit waveforms at the fundamental frequency, where they exhibit the three-phase voltage and three-phase load current, which varies smoothly at 60 Hz. Then the SM capacitor voltages are balanced with a $\pm 8\%$ voltage ripple. This voltage ripple value is achieved with a 15 μF film capacitor. Meanwhile, conventionally, a 1000 μF is needed for the same ripple. The figure also shows that the DC source produces a pure DC current. Additionally, it shows the MMC arm current for phase A. It can be seen that the arm currents are free from the 120 Hz and 240 Hz components. Therefore, the circulating current is almost a pure DC current. Figure 10 shows the performance of the proposed scheme at a 50% imbalance between the HFT leakage inductances. The proposed

Table 1 Simulation circuit parameter values

| Parameter	Value
Output active power	1 MW
SM capacitor voltage	2.5 kV
Fundamental line frequency	60 Hz
Switching frequency	15 kHz
Load resistance	$1.9 \times \frac{f}{60}\,\Omega$
Load inductance	2.1 mH
Arm inductance	1.5 mH
Equivalent SM capacitance	15 μF
HFT turns ratio	1:1:1
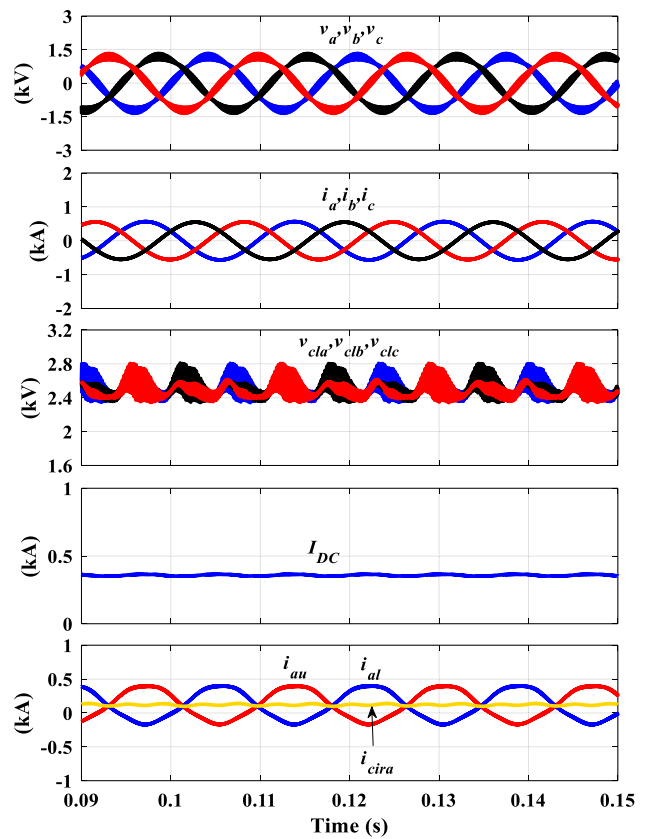
Fig. 9 Simulation waveforms of the proposed scheme under its rated parameters

sliding mode control succeeded in compensating the imbalance, which results in the SM capacitor voltage ripples being balanced. The simulation investigated the robustness of the proposed control against circuit parameter variations.
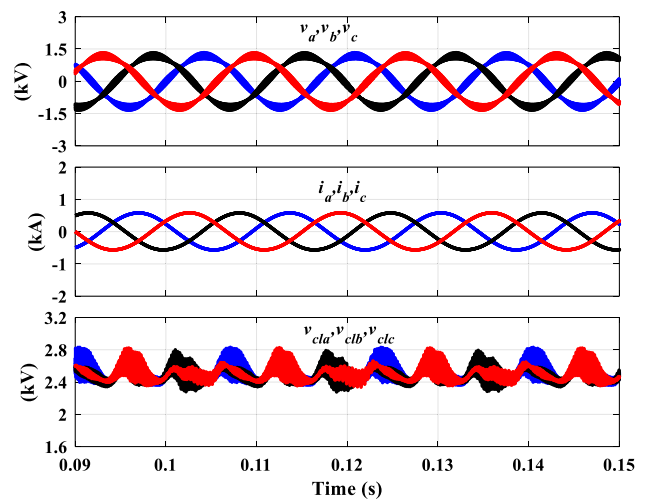
Fig. 10 Performance of the proposed scheme at a 50% imbalance in the HFT leakage inductances
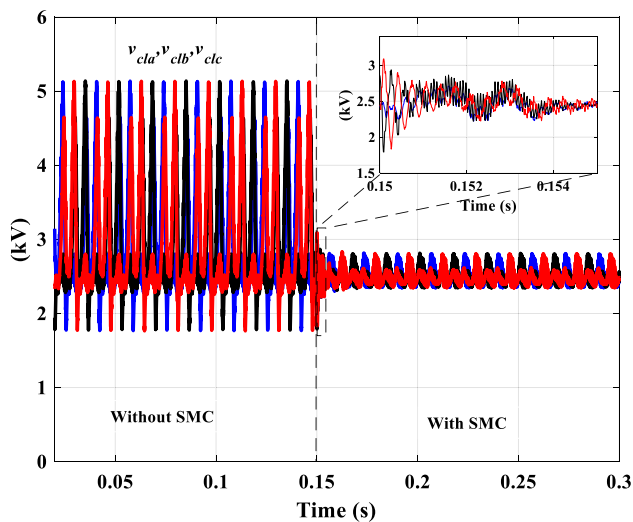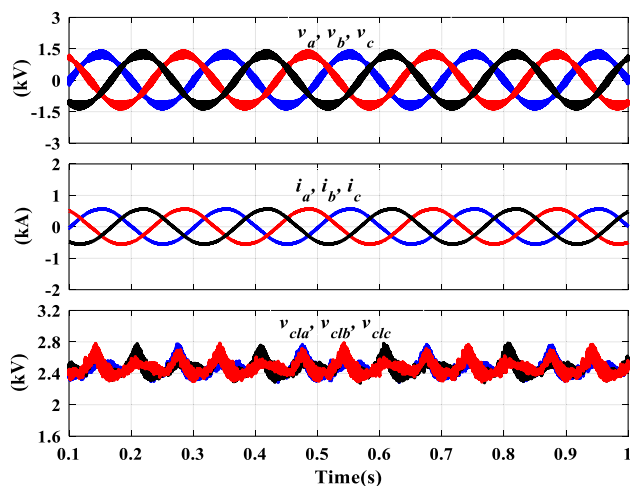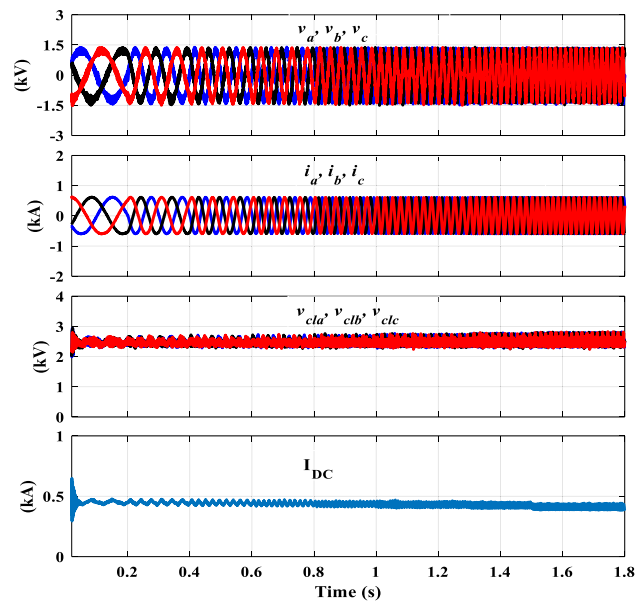
Fig. 11 Simulation waveforms of SM capacitor voltages with and without the sliding mode control (SMC)

Fig. 13 Transient response of the proposed scheme under continuous frequency variations

Figure 11 shows SM capacitor voltage waveforms with and without the sliding mode control (SMC). The circuit started without the SMC. Then at 0.15 s, the sliding mode control is activated. The transient time is less than half of a cycle of the fundamental frequency with negligible overshoot and undershoot. The proposed control compensated more than 88% of the SM capacitor voltage ripple with a significantly small settling time. This cannot be achieved with normal ripple rejection control due to bandwidth limitations.

The main enhancement of the proposed scheme is replacing the low-frequency SM capacitor with a frequency-independent power decoupling scheme, which solves the issue of wide voltage fluctuations in the SM capacitor under low-speed operation. To investigate this, the circuit was tested

Fig. 12 Performance of the proposed scheme under a 5 Hz fundamental line frequency

under low-frequency operation at a constant load current. The load resistance was changed linearly to keep the load current constant, which represents the constant torque condition. The control parameters were maintained the same without any change as the rated frequency control parameters. Figure 12 shows circuit waveforms at a 5 Hz operating frequency.

They indicate that the THB power decoupling scheme can keep the voltage ripple constant ($\pm 8\%$) under a near-zero-speed operation. This voltage ripple is achieved with a 15 µF film capacitor, while a 12,000 µF is normally needed at 5 Hz. Employing the proposed scheme reduces the required SM capacitance. Figure 13 shows the dynamic performance of the proposed scheme when driving a 3-phase machine from standstill to full speed under a constant torque condition. The SM capacitor voltage ripple is nearly constant over a wide range of frequency variations. The proposed scheme shows a very smooth transient response with a negligible transient time.

4.2 Experimental verification

A hardware prototype was built to validate the proposed scheme. All of the MMC-SM capacitors in the circuit were metalized-polypropylene film-type capacitors from Vishay, with a capacitance of 30 µF and a rating of 500 V DC. The load power for the three phases was 1.3 kW. All of the switches used in the circuit were silicon-carbide switches chosen to improve efficiency. Two lab-made high-frequency transformers with 1:1:1 turn ratios were used with a sandwich winding method. Six 100 µH inductors were connected

Table 2 Experimental circuit parameter values

Parameter	Value
Output active power	1.3 kW
SM capacitor voltage	260 V
Line frequency	60 Hz
Carrier frequency	15 kHz
Load resistance	$19 \times \frac{f}{60} \, \Omega$
Arm inductance	1.5 mH
equivalent SM capacitance	15 µF
HFT turns ratio	1:1:1
The leakage inductance	100 µH
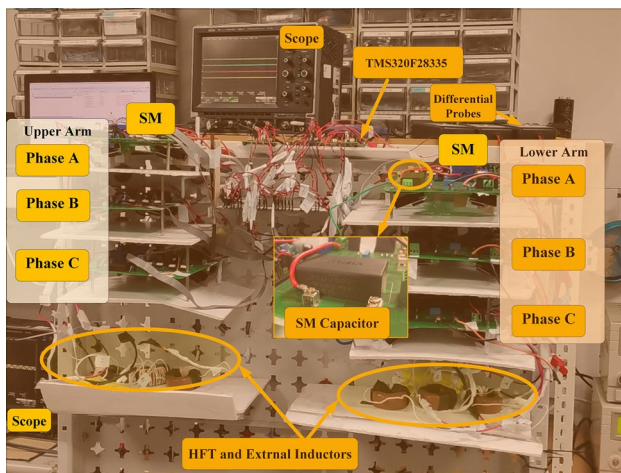
Fig. 14 Lab prototype circuit

Fig. 15 Experimental waveforms of the proposed scheme under its rated parameters

in series with transformer windings. The control configurations were implemented on a TMS320F28335 with an XDS100v1 development board. Detailed information on the prototype is listed in Table 2, and the circuit setup is shown in Fig. 14.

To highlight the enhancement of the proposed MMC scheme, the circuit has been tested under a low operating frequency (Figs. 15, 16 and 17). Figures 18 and 19 show circuit waveforms at 30 Hz and 10 Hz converter line frequencies, respectively. The load current is regulated to be constant at the different operating frequencies. The control parameters are kept the same without any changes of the rated frequency control parameters. The SM capacitor voltage ripples are ± 8.49% and ± 9.43% at 30 Hz and 10 Hz, respectively. Figure 20 shows experimental waveforms at a 5 Hz operating frequency. This figure shows that the SM capacitor voltage ripples are ± 10% under near-zero-speed operating. These voltage ripples are achieved with an SM capacitance of 15 µF. There is very little high-frequency chattering in the SM voltage due to the sliding mode control
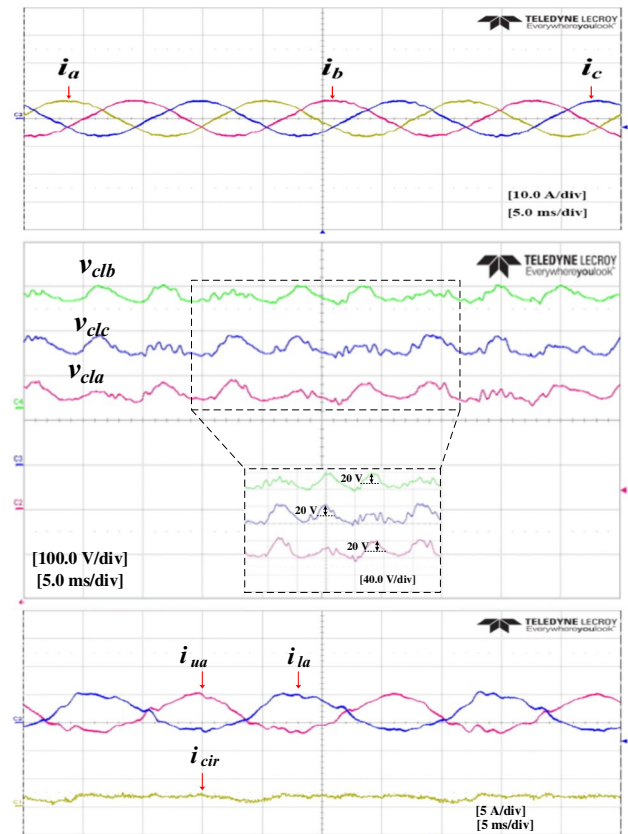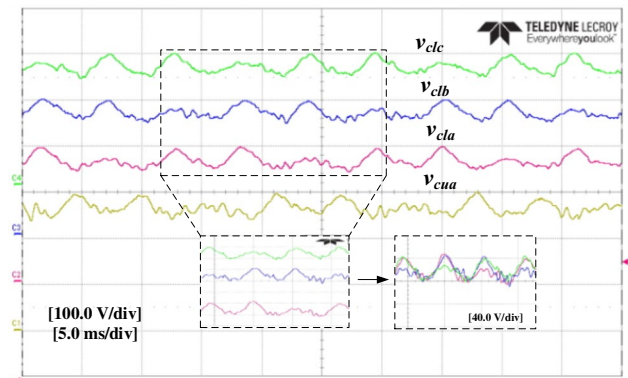
Fig. 16 Experimental waveforms of SM capacitor voltages under HFT external inductors $L_a = 100$ µH, $L_b = 100$ µH, and $L_c = 75$ µH

action. The SM capacitor voltage ripple is nearly constant over a wide range of frequencies.

Figure 21 shows power decoupling circuit-based THB waveforms under the rated operation conditions. The HFT current contains the switching frequency component with
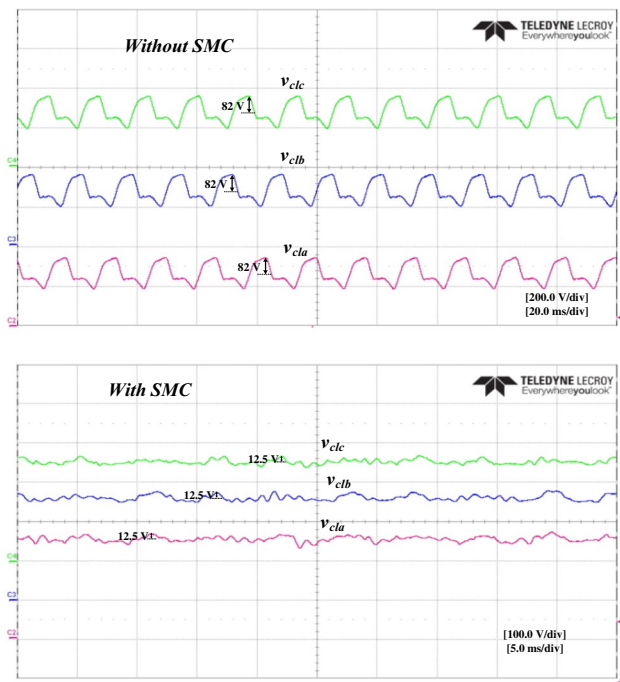
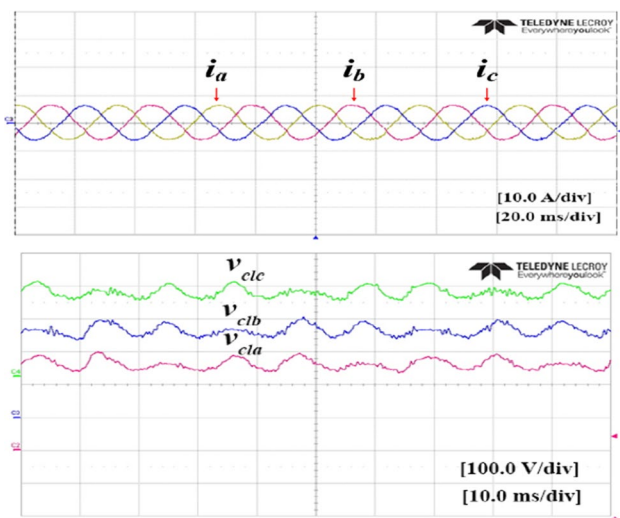**Fig. 17** Experimental waveforms of SM capacitor voltages with and without the sliding mode control (SMC)

Fig. 18 Experimental waveforms of the proposed scheme under a 30 Hz fundamental line frequency

Fig. 19 Experimental waveforms of the proposed scheme under a 10 Hz fundamental line frequency
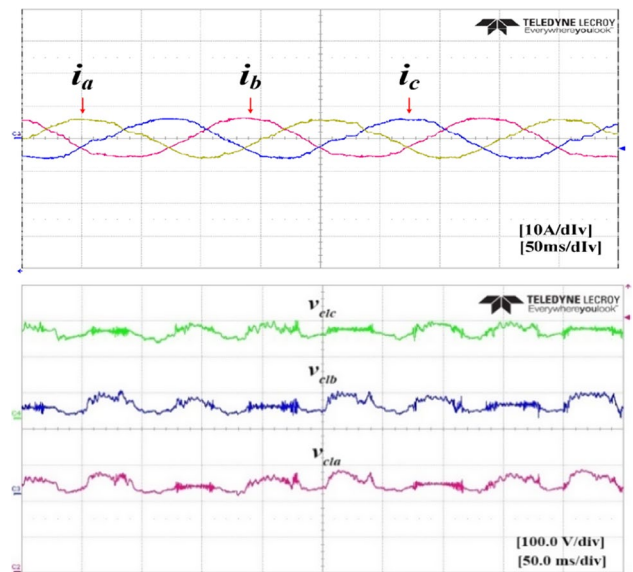
Fig. 20 Experimental waveforms of the proposed scheme under near-zero-speed operation

a low-frequency envelop. The low-frequency components are transferred to be canceled out in the transformer core. This demonstrates that the power decoupling circuit works as expected. The switching component of the transformer currents shows that the proposed sliding mode control works as expected sinc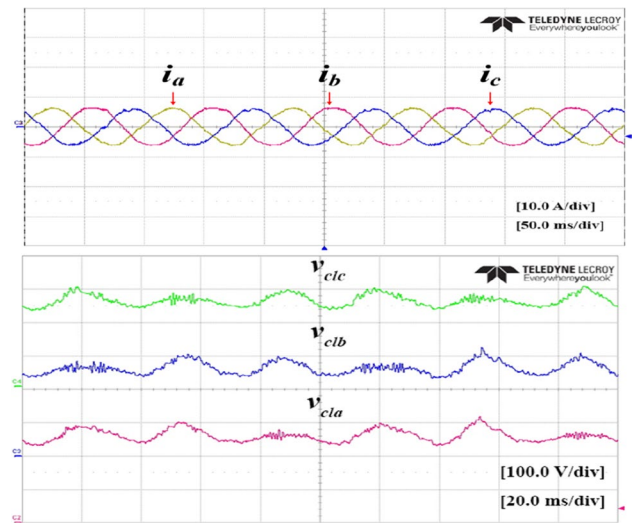e the three currents have the fundamental waveform at the switching frequency, and are shifted to cause the transformer to absorb more voltage ripple. The transformer rated current is nearly half the phase current, which demonstrates the quality of the proposed scheme.

5 Discussion

In this section, circuit volumes are used for a comparison of the proposed scheme, two other schemes [9, 10], and the conventional MMC. The design specifications for the four
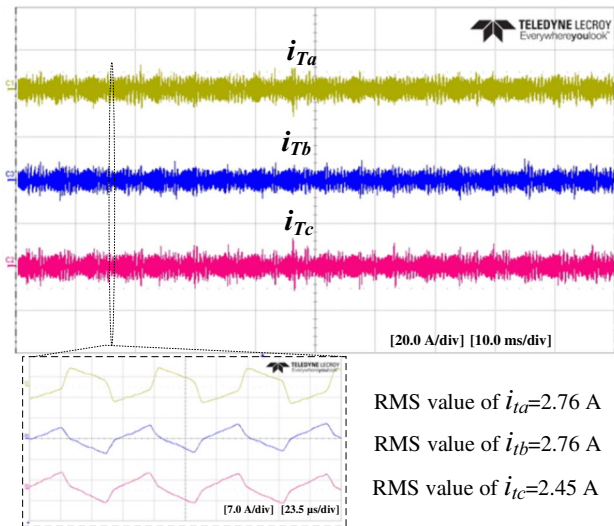
Fig. 21 Experimental waveforms of HFT currents under its rated parameters

Fig. 22 Component volume comparison per SM of the proposed scheme, the scheme in [9], the scheme in [10], and the conventional MMC

topologies are a $\pm$ 5% voltage ripple at a near-zero speed, a total power of 10 MW, and an average SM voltage of 2.5 kV. The results for one sub-module are shown below.

For a conventional MMC, a 13 mF, 2500 V SM capacitor is required [9]. A 1300 µF, 1320 V capacitor (TDK) with a volume of 14.84 L is commercially available, which means the total volume of the required capacitors is 593.6 L [28].

Two 2 mF, 1300-V SM capacitors are needed for the topologies in [9] and [10]. Using the aforementioned commercial capacitors, the total volume of the capacitors is 59.36 L. This represents a 90% reduction in capacitor volume relative to the conventional MMC. However, for the proposed scheme, two 30 µF, 1300 V SM capacitors are required. A 30 µF, 1400 V capacitor (CDE) with a volume of 0.3 L is commercially available [29]. The total volume of the capacitors is 1.2 L, which represents a 99% reduction in the capacitor volume (again relative to conventional MMCs).

In [10], the power decoupling branch has four semiconductor switches, and 5SNA0650J450300 IGBTs (4.5 kV, 650 A, ABB) are used. The volume of one IGBT is 0. 87 L, and the total volume of the switches in the power decoupling branch is 3.48 L. In both [9], and the proposed scheme, the power decoupling branch has two semiconductor switches. Therefore, the total volume of the switches in the power decoupling branches is 1.74 L. 5SNA1200G450350 IGBT semiconductors (4.5 kV, 1200 A, ABB) are used for the MMC branch, and the volume of one IGBT is 1.28 L. Thus, the total volume of the switches in the MMC branch is 2.56 L. The total volume of the switches in the conventional MMC is 2.56 L, and the overall switch volume in [10] is 6.04 L. Thus, the switching device volume is increased by 136% when compared to a conventional MMC. However, in [9] and in the proposed scheme, the overall switch volume is
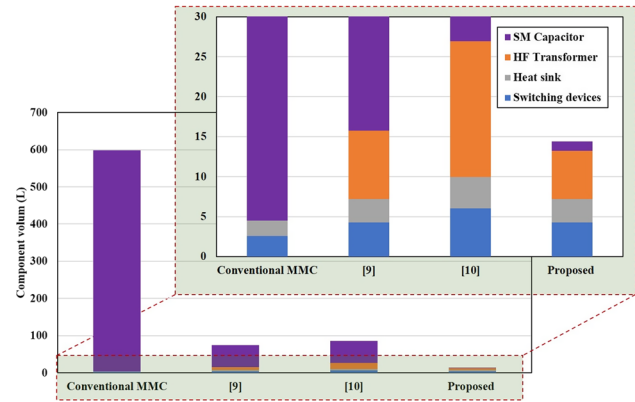
4.3 L. Therefore, the switching device volume is increased by 68% over that of a conventional MMC.

In [10], each of the SMs requires an HF transformer. In [9], the two submodules use an HF transformer. In the proposed scheme, each of the three SMs requires a HF transformer. The design procedures of the HF transformer for MV and high-power applications are discussed in [30], where it is noted that the transformer specifications are 1.25 kV, 330 A, and 17 L. Therefore, the transformer volume requirements for the topologies in [9, 10] and the proposed scheme are 8.5 L, 17 L, and 6 L, respectively.

Figure 22 shows a comparison of the component volumes for the four topologies with SM component switching devices (IGBT), IGBT heat sinks, HF transformers, and SM capacitors. The proposed scheme, [9], and [10] reduce the overall volume of the conventional MMC by 97%, 88%, and 86%, respectively. This reduction in the system volume is due to eliminating the LF SM capacitor.

6 Conclusion

A medium-voltage high-power machine drive system has been proposed based on a MMC with a three-port power decoupling approach. The proposed scheme solves the issue of the low-frequency ripple components in the sub-module (SM) capacitor voltage, where their magnitude is inversely proportional with respect to the converter line frequency, which limits employing a MMC in applications operating at a low-speed. The power decoupling approach employs a THB converter to extract the three-phase ripple power from the SMs. Then it delivers this power to the three-winding high-frequency transformer where the three-phase ripple power is dissipated magnetically regardless of the ripple frequency. To ensure that the SM capacitor voltage has

acceptable ripple components, a ripple rejection-based sliding mode control has been proposed. The proposed control is independent of the converter line frequency. Therefore, it is suitable for adjustable-speed applications. The proposed control shows a fast transient response with negligible overshoots and undershoots at continuous speed adjusting, which overcomes conventional methods drawbacks, such as bandwidth limitations and frequency dependence. The main advantages of employing the proposed scheme can be summarized as follows. (1) The proposed scheme is suitable for low-speed and continuous adjusting speed operations. (2) The proposed scheme is totally free from SM ripple power capacitors. Therefore, a significant reduction in the overall volume of the system is possible in comparison to conventional MMCs. (3) In fault cases, the possibility of the switching devices exploding is small since there are no large energy storage units in the circuit and the inrush current is small. (4) The proposed scheme succeeds in keeping the SM capacitor voltage ripple narrow regardless of the converter line frequency. (5) The proposed scheme is believed to be the best solution for variable-speed drives based on MMCs. It has the lowest rated and the smallest number of circuit components among the related SM ripple power decoupling methods. In addition, it does not increase the magnitude of the arm current relative to those of other circulating current injection techniques. The performance of the proposed scheme has been verified for MV high-power variable-speed applications with simulations and downscaled hardware experiments under various operating conditions.

References

1. Le, D.D., Lee, D.-C.: Current stress reduction and voltage total harmonic distortion improvement of flying-capacitor modular multilevel converters for AC machine drive applications. IEEE Trans. Ind. Electron. **69**(1), 90–100 (2022)
2. Perez, M.A., Ceballos, S., Konstantinou, G., Pou, J., Aguilera, R.P.: Modular multilevel converters: recent achievements and challenges. IEEE Open J. Ind. Electron. Soc. **2**, 224–239 (2021)
3. Ali, S., Ling, Z., Tian, K., Huang, Z.: Recent advancements in submodule topologies and applications of MMC. IEEE J. Emerg. Select. Top. Power Electron. **9**(3), 3407–3435 (2021)
4. Ke, Z., et al.: Capacitor voltage ripple estimation and optimal sizing of modular multi-level converters for variable-speed drives. IEEE Trans. Power Electron. **35**(11), 12544–12554 (2020)
5. Du, S., Wu, B., Tian, K., Zargari, N.R., Cheng, Z.: An active cross connected modular multilevel converter (AC-MMC) for a medium voltage motor drive. IEEE Trans. Ind. Electron. **63**(8), 4707–4717 (2016)
6. Du, S., Wu, B., Zargari, N., Cheng, Z.: A flying-capacitor modular multilevel converter (FC-MMC) for medium-voltage motor drive. IEEE Trans. Power Electron. **32**(3), 2081–2089 (2017)
7. Kong, Z., Huang, X., Wang, Z., Xiong, J., Zhang, K.: Active power decoupling for submodules of modular multilevel converter. IEEE Trans. Power Electron. **33**(1), 125–136 (2018)
8. Tang, Y., Chen, M., Ran, L.: A compact MMC submodule structure with reduced capacitor size using the stacked switched capacitor architecture. IEEE Trans. Power Electron. **31**(10), 6920–6936 (2016)
9. Diab, M.S., Massoud, A.M., Ahmed, S., Williams, B.W.: A dual modular multilevel converter with high-frequency magnetic links between submodules for MV open-end stator winding machine drives. IEEE Trans. Power Electron. **33**(6), 5142–5159 (2018)
10. Diab, M.S., Massoud, A.M., Ahmed, S., Williams, B.W.: A modular multilevel converter with ripple-power decoupling channels for three-phase MV adjustable-speed drives. IEEE Trans. Power Electron. **34**(5), 4048–4063 (2019)
11. P.J. Hu, A. Ahmed, M.S. Irfan, Multi-phase inverter using independent-type multi H-bridge, Korean Patent, 1018625170000, May, 05.2018 available at database of http://engpat.kipris.or.kr/engpat/searchLogina.do?next=MainSearch.
12. C. Liu, J.S. Lai, Low frequency current ripple reduction technique with active control in a fuel cell power system with inverter load. In: 2005 IEEE 36th Power Electronics Specialists Conference, pp. 2905–2911. IEEE, 2005.
13. Wang, J., Ji, B., Lu, X., Deng, X., Zhang, F., Gong, C.: Steady-state and dynamic input current low-frequency ripple evaluation and reduction in two-stage single-phase inverters with back current gain model. IEEE Trans. Power Electron. **39**(8), 4247–4260 (2014)
14. Zhang, L., Ren, X., Ruan, X.: A bandpass filter incorporated into the inductor current feedback path for improving dynamic performance of the front-end DC–DC converter in two-stage inverter. IEEE Trans. Ind. Elect. **61**(5), 2316–2325 (2014)
15. Cao, L., Loo, K.H., Lai, Y.M.: Systematic derivation of a family of output-impedance shaping methods for power converters—A case study using fuel cell-battery-powered single-phase inverter system. IEEE Trans. Power Electron. **30**(10), 5854–5869 (2015)
16. Cao, L., Loo, K.H., Lai, Y.M.: Output-impedance shaping of bidirectional DAB DC-DC converter using double-proportional-integral feedback for near-ripple-free DC bus voltage regulation in renewable energy systems. IEEE Trans. Power Electron. **31**(3), 2187–2199 (2016)
17. Kousalya, V., Rai, R., Singh, B.: Sliding model-based predictive torque control of induction motor for electric vehicle. IEEE Trans. Ind. Appl. **58**(1), 742–752 (2022)
18. Chakraborty, R., Samantaray, J., Dey, A., Chakrabarty, S.: Capacitor voltage estimation of MMC using a discrete-time sliding mode observer based on discrete model approach. IEEE Trans. Ind. Appl. **58**(1), 494–504 (2022)
19. Mohanty, P.R., Panda, A.K.: Fixed-frequency sliding-mode control scheme based on current control manifold for improved dynamic performance of boost PFC converter. IEEE J. Emerg. Sel. Top Power Electron. **5**(1), 576–586 (2017)
20. Chincholkar, S.H., Chan, C.-Y.: Design of fixed-frequency pulse width-modulation-based sliding-mode controllers for the quadratic boost converter. IEEE Trans. Circuits Syst. II Express Briefs **64**(1), 51–55 (2017)
21. Deivasundari, P., Uma, G., Poovizhi, R.: Analysis and experimental verification of Hopf bifurcation in a solar photovoltaic powered hysteresis current-controlled cascaded-boost converter. IET Power Electron **6**(4), 763–773 (2013)
22. Fu, D., Zhao, X., Zhu, J.: A novel robust super-twisting nonsingular terminal sliding mode controller for permanent magnet linear synchronous motors. IEEE Trans. Power Electron. **37**(3), 2936–2945 (2022)

23. Ahmed, A., Ganeshkumar, P., Park, J.-H., Lee, H.: FPGA-based centralized controller for multiple PV generators tied to the DC bus. J. Power Electron. **14**(4), 733–741 (2014)

24. Ahmed, A., Li, R.: Precise detection and elimination of grid injected DC from single phase inverters. Int. J. Precis. Eng. Manuf. **13**(8), 1341–1347 (2012)

25. Tawfik, M.A., Ahmed, A., Park, J.-H.: Double boost power-decoupling topology suitable for low-voltage photovoltaic residential applications using sliding-mode impedance-shaping controller. J. Power Electron. **19**(4), 881–893 (2019)

26. Yazdani, A., Iravani, R.: Voltage-Sourced Converters in Power Systems, vol. 34. Wiley, Hoboken (2010)

27. Trabelsi, R., Khedher, A., Mimouni, M.F., M'sahli, F.: Backstepping control for an induction motor using an adaptive sliding rotor-flux observer. Electr. Power Syst. Res. **93**, 1–15 (2012)

28. https://www.tdk-electronics.tdk.com/inf/20/50/ds/B2562_.pdf

29. https://www.cde.com/resources/catalogs/944U.pdf

30. Hurley, W.G., Woelfle, W.H.: Transformers and Inductors for Power Electronics—Theory, Design, and Applications. Wiley, New York (2013)

Chungu Lee received his B.S. degree from the Department of Electrical Engineering, Soongsil University, Seoul, Korea, in 2015, where he is presently working toward his combined M.S. and Ph.D. degrees in the Department of Electrical Engineering. His current research interests include the analysis and design of pulse width modulation switching converters and renewable energy applications, battery management systems, and the detection of battery fault issues.

Mohamed Atef Tawfik received his B.S. degree from the Department of Electrical Engineering, Assiut University, Asyut, Egypt, in 2013; and his M.S. degree in Electrical Engineering from Soongsil University, Seoul, South Korea, in 2020, where he is presently working toward his Ph.D. degree. He worked as Research Assistant in the Department of Renewable Energy of Desert Research Center, Cairo, Egypt, from 2014 to 2018. His current research interests include the analysis and design of switching power converters for renewable energy applications.

Ashraf Ahmed received his B.S. degree in Electrical Engineering from Assiut University, Assiut, Egypt, in 1999; and his M.S. degree from Cairo University, Cairo, Egypt in 2005; and his Ph.D. degree in the field of renewable energy control and power electronics from the University of Durham, Durham, ENG, UK, in 2011. He is presently working as an Assistant Professor at Soongsil University, Seoul, Korea. His current research interests include the analysis and design of switching power converters for renewable energy applications.

Mohammad Sameer Irfan received his B.S. degree in Electrical Engineering, and his M.S. degree in Power System and Drives from the Aligarh Muslim University, Uttar Pradesh, India, in 2004 and 2008, respectively. He received his Ph.D. degree from Soongsil University, Seoul, South Korea, in 2020. His current research interests include the analysis, design, and applications of dc- dc converters and renewable energy applications.

Joung-Hu Park received his B.S., M.S., and Ph.D. from the Department of Electrical Engineering and Computer Science of Seoul National University, Seoul, Korea, in 1999, 2001 and 2006, respectively. He is presently working as an Associate Professor at Soongsil University, Seoul, Korea. From August 2004 to August 2005, he was a Visiting Scholar at Virginia Tech. Blacksburg, VA, USA; and from July 2015 to June 2016, he was a Visiting Assistant Professor at the University of British Columbia, Vancouver, BC, Canada. His current research interests include the analysis of high-frequency switching converters and renewable energy applications.